China Instrument and Control Society
Instrumentation
INSTRUMENTATION, Vol. 13, No. 2, June 2026
https://doi.org/10.15878/j.instr.202600394

Article

A Fully-Actuated Pose Adjustment Method for Wing-Fuselage Assembly via Point-Cloud Gap Optimization

Xiao Xu[1,2], Yang Zhang[1,2], Runze Liu[1,2*], Haoyu Wu[1,2], Qihang Chen[1,2], Yongkang Lu[1,2], Wei Liu[1,2]

[1] School of Mechanical Engineering, Dalian University of Technology, Dalian, Liaoning, 114024, China

[2] State Key Laboratory of High-performance Precision Manufacturing, Dalian University of Technology, Dalian, Liaoning, 114024, China

[*] Corresponding author email: jxlrz2024@mail.dlut.edu.cn

Abstract: Wing-fuselage assembly is a critical process in aircraft manufacturing, and the gap distribution of the wing-fuselage assembly frames directly determines the stress state of the connection interface and the structural load-carrying capacity after assembly. However, most existing pose adjustment methods either do not consider the global gap distribution or optimize the gap only based on theoretical computer-aided design (CAD) models, making it difficult to effectively control the actual gap distribution under real manufacturing errors. In addition, traditional positioners adopt a master-slave driving mode, in which passive axes suffer from following errors due to the lack of independent control, thereby limiting the execution accuracy of pose adjustment. To address these problems, this paper proposes a fully-actuated pose adjustment method for wing-fuselage assembly via point-cloud gap optimization. First, point cloud data of the wing-fuselage assembly frames in a unified assembly coordinate system are obtained through laser scanning combined with Enhanced Reference System (ERS) reference point registration. Assembly gaps are then defined along prescribed region-wise assembly directions, and a multi-surface global gap evaluation model is established. Second, a two-stage optimization strategy combining coarse pre-alignment and fine pose adjustment is adopted, in which insertion-depth correction is decoupled from rotational gap-uniformity optimization to solve the optimal target assembly pose. Finally, the optimized pose is converted into multi-axis synchronous motion commands for fully-actuated positioners through fifth-order polynomial trajectory planning and inverse kinematic mapping, and the force-position data of the positioners are effectively monitored throughout the pose adjustment process. The proposed method is compared with a traditional manual assembly method on a wing-fuselage assembly experimental platform. The results show that the proposed method reduces the in-plane gap standard deviations of the upper and right assembly surfaces from 2.19 mm and 1.34 mm to 1.70 mm and 1.04 mm, respectively, significantly improving gap uniformity. Meanwhile, the positioner motion remains continuous and smooth during pose adjustment, and no abnormal force fluctuations occur at the support points. The proposed method provides an integrated and executable solution for high-precision wing-fuselage assembly by linking measured-point-cloud-based global gap optimization, fully-actuated pose adjustment, and real-time force-position monitoring, thereby supporting assembly safety assessment and quality traceability.

Keywords: wing-fuselage assembly; 3D point cloud measurement; assembly gap; pose optimization; fully-actuated pose adjustment

Citation: Xiao Xu, Yang Zhang, Runze Liu, Haoyu Wu, Qihang Chen, Yongkang Lu, Wei Liu."A Fully-Actuated Pose Adjustment Method for Wing-Fuselage Assembly via Point-Cloud Gap Optimization." Instrumentation 13, no. 2 (June 2026). https://doi. org/10.15878/j. instr.202600394

1 Introduction

In the assembly process of large aircraft components, wing-fuselage assembly is the most critical step, as its assembly quality directly affects the aerodynamic accuracy and long-term service reliability of the entire aircraft[1,2]. The assembly gap between the wing and the fuselage assembly frame directly reflects the geometric alignment of the assembly surfaces. If the gap distribution is uneven, it may result in excessive local gaps, local interference, or forced assembly, which in turn affects the load transfer path and stress distribution at the connection interface, thereby reducing structural assembly quality and long-term service reliability[3].

However, current engineering practices typically rely on a limited number of key measurement points to evaluate component pose and repeatedly adjust the pose based on manual experience until these key points satisfy the prescribed tolerances[1]. This strategy does not explicitly control the global gap distribution over the assembly surfaces. Although some studies consider gap distribution during wing-fuselage assembly, gap evaluation and pose optimization are still performed using theoretical computer-aided design (CAD) models, without fully accounting for manufacturing and machining deviations. Consequently, the optimized pose may not accurately reflect the actual gap distribution of the mating interfaces.

Furthermore, even when the target pose is determined by considering gap distribution, execution errors may still arise from the driving mechanisms of conventional pose-adjustment positioners. Existing positioners generally adopt a master-slave driving mode, in which only some axes are actively controlled while the remaining axes passively follow. Owing to friction and structural compliance, the passive axes cannot accurately reproduce the commanded motion, causing the achieved pose to deviate from the optimized target pose and consequently compromising the intended gap distribution. Therefore, there is an urgent need to develop a fully-actuated, high-precision wing-fuselage pose adjustment and assembly method that optimizes the global assembly-gap distribution based on the actual interface geometry of the wing and fuselage assembly frames.

To address the above problems, laser scanning technology can be used to acquire measured point clouds of the joining surfaces of the wing and fuselage assembly frames, and accurate assembly gap calculation can be achieved by reconstructing their three-dimensional geometry. In recent years, aviation assembly gap measurement based on 3D scanning and point-cloud processing has become an important means of assembly quality evaluation[3]. Scholars have conducted a series of studies on assembly gap calculation based on measured point clouds. Long et al. realized automatic measurement of aircraft skin gaps and flushness using 3D point clouds, including seam-region extraction as well as gap and flush calculation[4]. Dai et al. proposed a hierarchical multi-structure fitting method for seam feature extraction from raw 3D point clouds of aircraft skins[5]. Wang et al. proposed a density-invariant registration method for multi-scan point clouds in aircraft measurement[6]. Wang et al. addressed the wing-fuselage assembly scenario by integrating laser tracker, 3D scanner, and photogrammetry data, and achieved assembly gap coordination through multi-constraint optimization[7]. After assembly gaps are calculated from measured point clouds, the optimized component pose must be further solved to ensure that the gap distribution in the actual assembly process is consistent with the optimized theoretical gap distribution. In this regard, Wang et al. proposed a pose-alignment-based gap control method for wing panel assembly, established a multi-region gap redistribution model with gap tolerance constraints, and adjusted the assembly pose by coordinating the gap values in different regions[8]. Sun et al. proposed a pose-alignment-based gap optimization method for aerospace composite panel assembly, in which the optimal pose satisfying the gap constraints was solved by constructing the mapping relationship between pose and gap[9]. Chang et al. constructed a manufacturing variation model for composite panels based on measured point clouds and considered the influence of the actual assembly process and contact interference on assembly deformation prediction, providing a reference for incorporating measured geometric errors into assembly quality prediction[10]. However, existing studies have not sufficiently considered a multi-surface global gap field defined along prescribed region-wise assembly directions. For complex joining objects with multi-surface structural features, such as wing-fuselage assembly frames, it is difficult to comprehensively constrain key indicators such as the average gap of each assembly surface, in-plane uniformity, minimum safety gap, and assembly depth, making it difficult to guarantee the optimality of the global gap state.

Second, to achieve high-precision pose adjustment and assembly of components and eliminate the influence of following errors in passive axes, a fully-actuated positioning method can be adopted, in which each axis of the pose-adjustment positioner is independently driven and controlled in a coordinated manner to ensure its motion accuracy[11-13]. However, when multiple positioners jointly support and drive the component during pose adjustment and assembly, insufficient motion synchronization among the axes may introduce local constraint interactions between positioners and generate internal forces at the support points, posing a risk of component damage[13]. Therefore, it is necessary to establish a coordinated motion trajectory planning method compatible with fully-actuated pose adjustment and to monitor the component force state and positioner motion state in real time, ensuring that the component

moves smoothly to the target pose and that the assembly process remains safe.

To address the above limitations, this paper proposes a fully-actuated pose adjustment method for wing-fuselage assembly via point-cloud gap optimization. Compared with conventional assembly technologies that determine the assembly pose from discrete key measurement points or nominal geometric models, the proposed method evaluates the actual multi-surface gap distribution from measured point clouds along prescribed region-wise assembly directions, thereby incorporating the geometric deviations of the mating surfaces into pose optimization. Instead of directly solving a strongly coupled six-degree-of-freedom optimization problem, a two-stage strategy is adopted, in which coarse pre-alignment is first performed and insertion-depth correction is subsequently decoupled from rotational gap-uniformity optimization, reducing the local search space and variable coupling. In addition, fully-actuated positioners are used to convert the optimized target pose into coordinated motion commands through trajectory planning and inverse kinematic mapping, avoiding the passive-axis following errors associated with conventional master-slave driving modes. The minimum-safety-gap constraint, together with real-time monitoring of position and three-dimensional support forces, further provides safeguards against potential local interference and abnormal motion during pose-adjustment execution. The main contributions of this paper are as follows:

(1) A method for global gap modeling in wing-fuselage assembly based on measured point clouds is proposed. Local gaps are defined as directional distances from points on the fuselage assembly surface to the wing assembly surface along their corresponding prescribed region-wise assembly directions. This overcomes the limitation of traditional discrete measurement methods, which struggle to fully characterize the overall gap distribution, and provides a reliable data foundation for global gap optimization.

(2) A two-stage pose optimization method combining coarse pre-alignment and fine pose adjustment is established. In the coarse pre-alignment stage, initial pose alignment is achieved by extracting the principal normal and axis directions of the assembly frame; in the fine pose adjustment stage, insertion-depth correction and rotational gap-uniformity optimization are decoupled and solved separately, ensuring convergence stability while maintaining optimization efficiency.

(3) A spatial trajectory planning and inverse kinematic mapping method based on fifth-order polynomial interpolation is established. The target pose is converted into smooth motion commands executable by multi-axis fully-actuated positioners, ensuring motion continuity and controllability during the pose adjustment process.

(4) A real-time data acquisition and visualization monitoring system for the fully-actuated wing-fuselage assembly process is developed. This system enables the synchronous acquisition and real-time visualization of positioner displacement and 3D force data, providing systematic support for assembly safety assessment and quality traceability.

The remainder of this paper is organized as follows: Section 2 constructs a global gap model for wing-fuselage assembly based on measured point clouds and employs a method combining coarse pre-alignment with fine pose adjustment to determine the target assembly pose; Section 3 establishes a method for multi-axis coordinated motion trajectory planning and inverse kinematic mapping for the fully-actuated positioner; Section 4 introduces the design of the real-time data acquisition, storage, and visualization monitoring system for the assembly process; Section 5 verifies the effectiveness of the proposed method through comprehensive experiments; Section 6 summarizes the paper.

2 Optimization of Assembly Pose Based on Measured 3D Point Clouds

During the wing-fuselage assembly process, the fuselage assembly frame serves as a fixed reference, while the wing is supported and driven by multiple fully-actuated positioners, enabling the wing assembly frame to be gradually inserted into the fuselage assembly frame and adjusted to the target assembly position, as shown in Fig. 1.

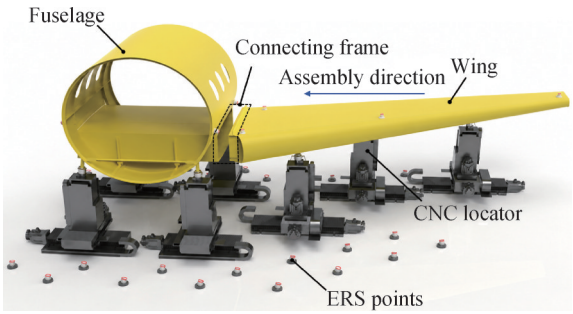

Fig.1 Schematic diagram of wing-fuselage assembly

The gap condition between the fuselage and wing assembly frames directly reflects the geometric alignment of the assembly surfaces. Based on measured point cloud data of the fuselage and wing assembly frames, this paper performs coordinate unification of multi-source point clouds and defines the directional gap of the assembly surfaces. By employing a method of coarse pre-alignment followed by fine pose adjustment, the target pose that satisfies the requirements for gap uniformity and safety gap is determined, providing input for subsequent trajectory planning and physical execution.

2.1 Acquisition of Measured Point Clouds and Unification of Assembly Coordinate Systems

To capture the true geometric configuration of the assembly surfaces between the fuselage and wing assembly frames, 3D scans were performed on the assembly surfaces of both the fuselage and wing assembly frames prior to wing-fuselage assembly, yielding point clouds of the assembly regions on both sides. Let the point clouds of the fuselage and wing assembly frames be denoted as:

$$P_f=\{p_{f,i}\,|\,i=1,2,\ldots,N_f\}$$

$$P_w=\{p_{w,j}\,|\,j=1,2,\ldots,N_w\}$$

where$p_{f,i}$and$p_{w,j}$denote spatial points in the fuselage and wing assembly frame point clouds, respectively, and N_f and N_w represent the number of points in the corresponding point clouds. Since the point clouds on both sides are typically acquired in different scanning coordinate systems, they must be unified into the assembly coordinate system before performing gap calculations and pose optimization.

This paper uses Enhanced Reference System (ERS) points placed on the ground or on the base of a positioning system as a common reference benchmark. ERS points are spatial reference points pre-deployed and calibrated at the assembly site; their coordinates in the aircraft component assembly coordinate system are known and can be used to establish a spatial transformation relationship between the scan coordinate system and the assembly coordinate system. Let the set of ERS points acquired in a given scan coordinate system be denoted as $E^s=\{e_k^s|k=1,2,\cdots,m\}$, and the corresponding set of points in the aircraft component assembly coordinate system be $E^a=\{e_k^a|k=1,2,\cdots,m\}$. Then, the rigid-body transformation from the scan coordinate system to the aircraft component assembly coordinate system can be expressed as:

$$p^a=Rp^s+t$$

where$R$ is the rotation matrix and$t$ is the translation vector. By minimizing the correspondence error of the ERS points, R and$t$ are solved:

$$\min_{R,t}\sum_{k=1}^{m}\left\| e_k^a-\left(Re_k^s+t\right)\right\|^2$$

After obtaining the coordinate transformation parameters, the point clouds of the fuselage and wing are respectively transformed into a unified assembly coordinate system. During the actual processing, the raw point clouds undergo preprocessing steps such as outlier removal, noise filtering, assembly-frame region segmentation, and downsampling. This reduces measurement noise and the impact of redundant points while preserving the overall topography of the assembly surfaces. The resulting valid point clouds are denoted as$\bar{p}_f$ and $\bar{p}_w$, respectively. All subsequent gap calculations and pose optimization are based on these valid point clouds.

2.2 Global Gap Definition Along Prescribed Assembly Directions

The cross-section of a wing-fuselage assembly frame typically exhibits a roughly curved rectangular configuration, in which the upper, lower, left, and right mating surfaces are associated with different local assembly directions. Although the cross-sectional geometry is relatively complex, the mating surfaces of the assembly frame can be divided into upper, lower, left, and right assembly-surface regions according to the nominal geometric configuration and mating relationships defined in the theoretical CAD model, with a well-defined region-wise assembly direction assigned to each region. Accordingly, the mating surfaces of the wing-fuselage assembly frame are partitioned into four regions. Let the effective point cloud of the fuselage corresponding to the k-th assembly surface region be:

$$\bar{P}_f^{(k)}=\{\bar{p}_{f,i}^{(k)}\,|\,i=1,2,\cdots,N_f^{(k)}\}$$

For any point $\bar{p}_{f,i}^{(k)}$ within the k-th assembly-surface region, let $d^{(k)}$ denote the unit assembly direction of that region, oriented from the fuselage mating surface toward the wing mating surface. All points within the same assembly-surface region are evaluated along the corresponding region-wise assembly direction.

The assembly gap at a point on the fuselage mating surface is defined as the length of the line segment obtained by extending a ray from that point along the assembly direction of its corresponding surface region toward the wing mating surface until it intersects the wing mating surface, as shown in Fig. 2. This gap is not the Euclidean shortest distance between the two point clouds in an arbitrary direction; instead, it is a directional distance defined along the region-wise assembly direction, which reflects the separation, proximity, or potential interference between the mating surfaces along the actual assembly-constraint direction.

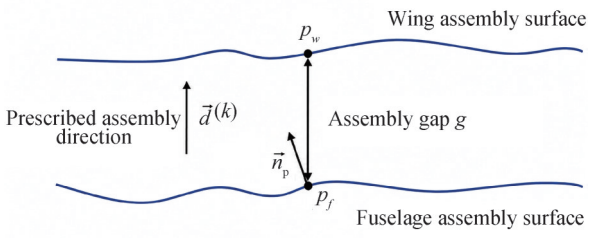

Fig.2 Gap definition along a prescribed region-wise assembly direction

For point $\bar{p}_{f,i}^{(k)}$, its assembly-direction ray can be expressed as:

$$\mathbf{r}_i^{(k)}(\lambda)=\bar{p}_{f,i}^{(k)}+\lambda d^{(k)},\quad \lambda\geq 0$$

If the intersection of this ray with the wing assembly surface is $p_{w,i}^{(k)}$, then the assembly gap at this point is:

$$g_i^{(k)}=\left\| p_{w,i}^{(k)}-\bar{p}_{f,i}^{(k)}\right\|$$

Equivalently, the intersection point can be expressed as:

$$p_{w,i}^{(k)}=\bar{p}_{f,i}^{(k)}+g_i^{(k)}d^{(k)}$$

when $g_i^{(k)}$ falls within the design tolerance range, it indicates that the assembly gap at that location is reasonable; when it is too small or approaches zero, it indicates that contact or potential interference exists in that area; when it is too large, it indicates that there is a problem of excessive local gap in that area. Based on the above definition, the directional gap at an individual point can be extended to a global gap field across the entire assembly area, thereby describing the magnitude of gap, distribution uniformity, and local anomalies in different regions of the assembly surfaces, providing a basis for subsequent point cloud gap calculations and pose optimization.

Several factors may affect the uncertainty of the directional-gap calculation. Let ε_r denote the residual registration error after transforming the fuselage and wing point clouds into the common assembly coordinate system, and let ε_s denote the error associated with surface representation and ray-surface intersection when determining the corresponding point on the wing mating surface. In addition, when a prescribed region-wise assembly direction is used to approximate the local mating direction, an angular mismatch $\Delta\theta$ may introduce a geometric discrepancy.

Under a local parallel-surface approximation, let g_{loc} denote the gap along the local mating direction. The scalar gap difference caused by the directional mismatch can be approximated as

$$\varepsilon_d \approx g_{\mathrm{loc}}(\sec\Delta\theta-1)$$

and the associated lateral offset can be expressed as

$$\delta_{\mathrm{lat}} \approx g_{\mathrm{loc}}\tan\Delta\theta$$

Accordingly, an engineering estimate of the directional-gap uncertainty is given by

$$\left|\delta g\right| \lesssim \varepsilon_r+\varepsilon_s+\varepsilon_d$$

The angular term does not alter the definition of the prescribed-direction gap; rather, it characterizes the potential geometric discrepancy when a region-wise direction is used to represent a rapidly varying local mating direction. Therefore, the directional-gap uncertainty remains limited when registration and intersection errors are controlled and the prescribed direction is close to the local mating direction.

The proposed region-wise directional-gap model is primarily applicable to assembly-frame structures whose mating surfaces can be partitioned into a finite number of regions with stable, process-defined assembly directions. For the wing-fuselage assembly frame considered in this study, the upper, lower, left, and right mating surfaces satisfy this condition, and the prescribed direction of each region is determined from the nominal mating relationship rather than from pointwise local-normal estimation. For joining structures with highly curved surfaces, rapidly varying local surface orientations, or ambiguous assembly directions, the assembly-surface partition should be further refined so that each subregion retains a sufficiently stable assembly direction. Where a region-wise directional representation is inadequate, the proposed gap model should be supplemented by local geometric analysis or a local-normal-based verification procedure. This applicability boundary should be considered when extending the proposed method to more complex joining configurations.

2.3 Multi-Surface Gap Optimization Method Based on Coarse Pre-Alignment and Fine Pose Adjustment

After unifying the point cloud coordinates and defining the directional gaps, it is necessary to determine the target assembly pose of the wing relative to the fuselage. Directly using six-degree-of-freedom translation and rotation parameters as optimization variables results in a large search space, strong coupling of the objective functions, and reduced convergence efficiency. To address this, this paper adopts a phased method combining coarse pre-alignment and fine pose adjustment: first, the coarse pre-alignment pose is obtained using the center of the assembly frame end face, the axis direction, and the assembly surface normal; subsequently, in the fine pose adjustment stage, overall insertion-depth correction is decoupled from gap-uniformity optimization. Translation is first applied along the overall insertion direction to reach the target insertion depth, followed by small-angle rotation optimization to improve the gap distribution across each assembly surface. The overall optimization process is shown in Fig. 3.

2.3.1 Construction of the Objective Function

First, assume that the fuselage and wing assembly frames are divided into K assembly surface regions, typically corresponding to the upper, lower, left, and right surfaces. Under a candidate pose, the set of directional gaps for the k-th assembly surface region is denoted as:

$$G^{(k)}(\mathbf{x})=\{g_i^{(k)}(\mathbf{x})\,|\,i=1,2,\cdots,N_g^{(k)}\}$$

where $\mathbf{x}$ are the candidate pose parameters, and $N_g^{(k)}$ is the number of valid gap points within that region. The average gap and the standard deviation of the in-plane gap for the k-th assembly surface are defined as:

$$\mu_g^{(k)}(\mathbf{x})=\frac{1}{N_g^{(k)}}\sum_{i=1}^{N_g^{(k)}}g_i^{(k)}(\mathbf{x})$$

$$\sigma_g^{(k)}(\mathbf{x})=\sqrt{\frac{1}{N_g^{(k)}}\sum_{i=1}^{N_g^{(k)}}\left[g_i^{(k)}(\mathbf{x})-\mu_g^{(k)}(\mathbf{x})\right]^2}$$

where $\mu_g^{(k)}$ reflects the overall gap level of the assembly surface, and $\sigma_g^{(k)}$ reflects the uniformity of the in-plane gap distribution. Let the target average gap of the k-th assembly surface be $g_0^{(k)}$; then, the target gap deviation term and the in-plane uniformity term are respectively:

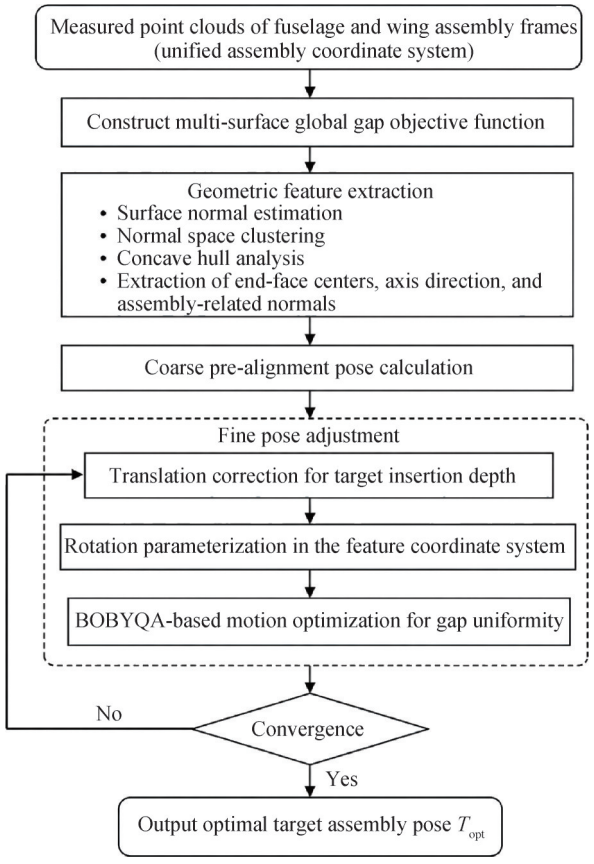

Fig.3 Multi-surface gap optimization process based on coarse pre-alignment and fine pose adjustment

$$J_g(\mathbf{x})=\sum_{k=1}^{K}\left[\mu_g^{(k)}(\mathbf{x})-g_0^{(k)}\right]^2,\quad J_\sigma(\mathbf{x})=\sum_{k=1}^{K}\left[\sigma_g^{(k)}(\mathbf{x})\right]^2$$

The overall insertion depth describes the extent to which the wing enters the fuselage assembly area along the overall insertion direction. Let the unit vector of the overall insertion direction be $\mathbf{d}_{\text{ins}}$, the position of the wing's center of features in the candidate pose be $\mathbf{c}_w(\mathbf{x})$, and the center of features of the fuselage assembly frame be $\mathbf{c}_f$. Then, the insertion depth is:

$$h(\mathbf{x})=\left[\mathbf{c}_w(\mathbf{x})-\mathbf{c}_f\right]^T\mathbf{d}_{\text{ins}}$$

The corresponding insertion depth evaluation term is:

$$J_h(\mathbf{x})=\left[h(\mathbf{x})-h_0\right]^2$$

To avoid the situation where the optimization process focuses solely on achieving an average gap close to the target value or uniform in-plane gap—which could lead to excessively small gaps or even interference in local regions—it is necessary to impose a constraint on the minimum safety gap. Let the minimum safety gap for the k-th assembly surface (k) be $g_s^{(k)}$. If the gap at a given point is less than this value, it indicates a risk of interference or insufficient assembly safety margin in that region. Accordingly, the safety gap penalty term is defined as:

$$J_s(\mathbf{x})=\sum_{k=1}^{K}\sum_{i=1}^{N_g^{(k)}}\left[\max\left(0,g_s^{(k)}-g_i^{(k)}(\mathbf{x})\right)\right]^2$$

Taking the above factors into account, we construct the multi-assembly-surface gap optimization objective function:

$$J(\mathbf{x})=w_gJ_g(\mathbf{x})+w_\sigma J_\sigma(\mathbf{x})+w_hJ_h(\mathbf{x})+w_sJ_s(\mathbf{x})$$

where w_g , w_σ , w_h , and w_s are the weight coefficients associated with the mean-gap-deviation term, in-plane gap-uniformity term, overall insertion-depth term, and minimum-safety-gap penalty term, respectively. Since both J_g and J_σ are constructed from squared gap quantities and therefore have the same physical dimension, $w_g=1$ and $w_\sigma=1$ are adopted in this study. During the subsequent fine-adjustment stage, the overall insertion depth is first corrected through translation along the assembly direction, and the mean-gap deviations are consequently reduced to a relatively small range. In comparison, the in-plane gap-uniformity term remains the primary objective improved through rotational adjustment. Therefore, under the same base weight, the optimization preferentially improves in-plane gap uniformity while preventing the mean gaps from deviating from their target values during rotation.

The overall insertion-depth coefficient is set to $w_h=1$. The insertion depth is corrected separately through translation along the assembly direction and is excluded from the subsequent rotation-only optimization. Since insufficient local gaps may lead to contact or interference, the minimum-safety-gap penalty coefficient is set to $w_s=1000$, such that candidate poses violating the minimum safety-gap requirement receive a substantial penalty. This weight configuration is specified for the assembly-frame configuration, point-cloud downsampling strategy, and assembly-process requirements considered in this study and remains unchanged throughout all optimization cases.

This objective function simultaneously considers the deviation of the mean gap of each assembly surface from its target value, the in-plane gap uniformity within each assembly surface, the overall insertion depth, and the minimum-safety-gap constraint. During subsequent fine adjustment, all variables are not optimized simultaneously in the six-degree-of-freedom space. Instead, the overall insertion-depth adjustment is separated from the gap-uniformity adjustment to reduce variable coupling.

2.3.2 Coarse Pre-alignment Based on Normal Clustering and Convex Hull Detection

The coarse pre-alignment stage is used to achieve initial alignment between the wing and fuselage assembly frames prior to fine pose adjustment, eliminating significant initial pose deviations and bringing the wing assembly frame into an initial assembly state close to the target insertion depth. This process provides reliable initial values for subsequent fine pose adjustment, narrows the gap optimization search range, and improves optimization stability and convergence efficiency.

First, normal vectors are estimated for the point

clouds of the fuselage and wing assembly surfaces. To improve the adaptability of normal vector calculations to variations in point cloud density, local noise, and boundary points, this study employs an adaptive neighborhood PCA method to estimate local normals and combines them with the theoretical assembly surface normals to correct for directional consistency. Based on this, a clustering method based on density peaks in normal space is used to partition the assembly surface point clouds into assembly surface regions. This method statistically analyzes the directional distribution of each point's normal on a unit sphere, extracts four primary density peak directions as the assembly surface principal normals, and performs point cloud clustering based on the principle of minimizing the angle between the point's normal and the principal normal. Specifically, the upper and lower assembly surfaces are determined based on the angle relationship between the principal normal and the Z-axis of the aircraft component assembly coordinate system; the left and right assembly surfaces are distinguished by combining the direction of the assembly frame axis. To improve the accuracy of axis direction calculation, this paper extracts the boundary points of the outer contour of the assembly frame cross-section using convex hull detection and determines the positive and negative directions of the axis based on the overall distribution of the point cloud, thereby obtaining the accurate direction of the assembly frame axis. For the fuselage and wing assembly frames, their average assembly surface normals are denoted as $\mathbf{n}_f^{(k)}$ and $\mathbf{n}_w^{(k)}$, respectively; the centers of the assembly frame end faces are $\mathbf{c}_f$ and $\mathbf{c}_w$; and the axis directions are $\mathbf{a}_f$ and $\mathbf{a}_w$.

The coarse pre-alignment rotation matrix R_c is determined by aligning the axis directions of the fuselage and wing assembly frames and the corresponding assembly surface normals:

$$R_c = \arg\min_{R\in SO(3)} \left[\omega_a \left\| R\mathbf{a}_w - \mathbf{a}_f \right\|^2 + \sum_{k=1}^{4} \omega_k \left\| R\mathbf{n}_w^{(k)} - \mathbf{n}_f^{(k)} \right\|^2 \right]$$

where ω_a and ω_k are the alignment weights for the axis direction and the assembly surface normal, respectively.

Since the fuselage assembly frame serves as a fixed reference during the assembly process, this paper uses the fuselage assembly frame axis direction $\mathbf{a}_f$ as the overall insertion direction for the wing-fuselage assembly. The insertion depth of the wing assembly frame relative to the fuselage assembly frame is characterized by the projection distance of the center points of both end faces along the $\mathbf{a}_f$ direction. After obtaining the coarse pre-alignment rotation matrix R_c, the target position $\mathbf{c}_w^{\text{target}}$ of the wing assembly frame end face center points is determined based on the target insertion depth h_0, thereby obtaining the pre-alignment translation t_c:

$$\mathbf{c}_w^{\text{target}} = \mathbf{c}_f + h_0\mathbf{a}_f, \quad t_c = \mathbf{c}_w^{\text{target}} - R_c\mathbf{c}_w$$

Therefore, the coarse pre-alignment transformation matrix is:

$$T_c = \begin{bmatrix} R_c & t_c \\ 0 & 1 \end{bmatrix}$$

After coarse pre-alignment, the wing point cloud is adjusted to a state close to the target insertion depth and consistent with the basic pose, thereby narrowing the search range for subsequent fine pose adjustment and improving the stability and efficiency of gap optimization.

2.3.3 Fine Pose Adjustment Strategy with Decoupled Insertion-Depth Correction and Gap-Uniformity Optimization

After coarse pre-alignment, the wing and fuselage assembly surfaces are already in a relatively close initial assembly state; however, issues such as inconsistent average gaps, uneven in-plane gap distribution, or excessively small local gaps may still exist on the assembly surfaces. In the fine pose adjustment stage, this paper adopts a "depth correction—gap uniformity optimization" decoupling strategy: in each iteration, the overall insertion depth is first adjusted to the target value via translational correction; then, the translation amount is fixed, and only the three small-angle rotation parameters are used as optimization variables to achieve gap uniformity optimization.

Let the wing pose at the start of the i-th iteration be:

$$T^{(r)} = \begin{bmatrix} R^{(r)} & t^{(r)} \\ 0 & 1 \end{bmatrix}$$

The insertion depth is:

$$h^{(r)} = \left[R^{(r)}\mathbf{c}_w + t^{(r)} - \mathbf{c}_f \right]^T \mathbf{a}_f$$

To achieve the target insertion depth, perform a minimum-norm translation correction along the overall insertion direction:

$$\Delta t_h^{(r)} = \left(h_0 - h^{(r)} \right)\mathbf{a}_f, \quad t^{(r)} = t^{(r)} + \Delta t_h^{(r)}$$

This step adjusts only the translation parameters and is restricted to the overall insertion direction, thereby avoiding the introduction of unnecessary lateral translation degrees of freedom due to the scalar constraint of insertion depth.

During the rotational fine pose adjustment stage, to enhance the correlation between rotational variables and changes in the assembly frame gap, this paper establishes an assembly frame feature coordinate system based on the axis directions and assembly surface normals extracted during the coarse pre-alignment stage, rather than directly using the X/Y/Z rotation angles in the global coordinate system. Let the axis direction of the fuselage assembly frame be $\mathbf{e}_a$; the lateral characteristic direction $\mathbf{e}_h$ is determined by the normals of the left and right assembly surfaces, and the vertical characteristic direction $\mathbf{e}_v$ is determined by the normals of the upper and lower assembly surfaces. After orthogonalization, the basis matrix of the characteristic coordinate system is constructed as follows:

$$B_f = \begin{bmatrix} \mathbf{e}_a & \mathbf{e}_h & \mathbf{e}_v \end{bmatrix}$$

The fine rotation variable $\boldsymbol{\omega}$ is defined as:

$$\boldsymbol{\theta}=\begin{bmatrix}\theta_a\\ \theta_h\\ \theta_v\end{bmatrix},\quad \boldsymbol{\omega}=B_f\boldsymbol{\theta}$$

where θ_a , θ_h , and θ_v represent small-angle rotations around the assembly frame axis, the lateral feature direction, and the vertical feature direction, respectively. This parameterization establishes a more direct correspondence between the rotation variables and the geometric structure of the assembly frame as well as changes in the gap.

Under the condition that the translation amount $\tilde{t}^{(r)}$ is fixed after depth correction, fine-tune the rotation of the wing around the current center of the assembly frame by a small angle. Let the center of the wing assembly frame after depth correction be:

$$\tilde{\mathbf{c}}_w^{(r)}=R^{(r)}\mathbf{c}_w+\tilde{t}^{(r)}$$

Then the coordinates of any point in the wing point cloud after fine pose adjustment are:

$$\bar{p}_{w,j}^{(r)}(\boldsymbol{\theta})=R_\Delta(\boldsymbol{\theta})\left[R^{(r)}\bar{p}_{w,j}+\tilde{t}^{(r)}-\tilde{\mathbf{c}}_w^{(r)}\right]+\tilde{\mathbf{c}}_w^{(r)}$$

where $R_\Delta(\boldsymbol{\theta})$ is the rotation matrix corresponding to the fine rotation variable$\boldsymbol{\omega}$. For a given$\boldsymbol{\theta}$, the directional gap sets $G^{(k)}(\boldsymbol{\theta})$ for the assembly-surface regions are recalculated, and the rotational fine-adjustment objective function is constructed as:

$$J_\theta(\boldsymbol{\theta})=w_gJ_g(\boldsymbol{\theta})+w_\sigma J_\sigma(\boldsymbol{\theta})+w_sJ_s(\boldsymbol{\theta})$$

Since the insertion depth has already been adjusted to meet the target requirements via translation correction at the start of this iteration, the depth term is no longer included in the rotation fine adjustment objective function. The rotation fine adjustment optimization problem is expressed as:

$$\boldsymbol{\theta}_{\text{opt}}^{(r)}=\arg\min_{\boldsymbol{\theta}}J_\theta(\boldsymbol{\theta}),\quad \boldsymbol{\theta}_{\min}\le\boldsymbol{\theta}\le\boldsymbol{\theta}_{\max}$$

where $\boldsymbol{\theta}_{\min}$ and $\boldsymbol{\theta}_{\max}$ are the lower and upper bounds of the rotation fine adjustment parameters, respectively, determined by the positioner's adjustment capability and the process-allowed angles.

After coarse pre-alignment and insertion-depth correction, the wing assembly frame is brought into a local search region close to the target assembly state. The rotational fine-adjustment stage therefore retains only three small-angle rotation variables defined in the assembly-frame feature coordinate system. For each candidate rotation parameter, the objective-function evaluation requires rigid transformation of the wing point cloud, recalculation of directional gaps in the assembly-surface regions, updating of local correspondence relationships, and evaluation of the minimum-safety-gap penalty. Because the local correspondence relationships and the ray–surface intersection states may change with the rotation parameters, and because the minimum-safety-gap term is piecewise penalized, a stable and reliable analytical gradient is difficult to obtain. In addition, finite-difference gradients may be sensitive to point-cloud noise and changes in local correspondence relationships.

Therefore, the rotational fine-adjustment problem is treated as a low-dimensional, bounded, derivative-free local optimization problem, and the Bound Optimization BY Quadratic Approximation (BOBYQA) algorithm is adopted for its solution. This algorithm constructs a local quadratic approximation within a trust region using only objective-function values and can directly handle variable-bound constraints[14].

In the *r*-th fine pose adjustment iteration, BOBYQA uses the current rotation increment $\boldsymbol{\theta}^l$ as the search center and selects several interpolation points within its neighborhood:

$$\boldsymbol{\theta}_j^l,\quad j=1,2,\cdots,m$$

For each interpolation point$\boldsymbol{\theta}_j^l$, a small rotation matrix $R_\Delta\boldsymbol{\theta}_j^l$ is constructed based on the feature coordinate system of the assembly frame. The positions of the wing point cloud are updated, and the set of assembly surface gaps $G^{(k)}(\boldsymbol{\theta}_j^l)$ is calculated according to the definition of assembly surface directional gaps, thereby obtaining the corresponding objective function value

$$J_\theta(\boldsymbol{\theta}_j^l),\quad j=1,2,\cdots,m$$

Subsequently, BOBYQA constructs a local quadratic approximation model $J_\theta(\boldsymbol{\theta})$ within the current search neighborhood based on the interpolation points and their objective function values:

$$Q_l(\boldsymbol{\theta})=c_l+\mathbf{g}_l^T(\boldsymbol{\theta}-\boldsymbol{\theta}^l)+\frac{1}{2}(\boldsymbol{\theta}-\boldsymbol{\theta}^l)^TH_l(\boldsymbol{\theta}-\boldsymbol{\theta}^l)$$

where $Q_l(\boldsymbol{\theta})$ represents the local quadratic model in the *l*-th BOBYQA iteration, c_l ,$\mathbf{g}_l$, andH_l are the constant term, linear term coefficient matrix, and quadratic term coefficient matrix determined by the function values at the interpolation points, respectively. This model is used to approximate the trend of the point cloud gap objective function within the current rotation parameter neighborhood.

Under the variable-bound and trust-region constraints, the optimal candidate rotation vector is obtained by solving the following subproblem:

$$\boldsymbol{\theta}_{\text{cand}}^l=\arg\min_{\boldsymbol{\theta}}Q_l(\boldsymbol{\theta})$$
$$\text{s.t.}\quad \boldsymbol{\theta}_{\min}\le\boldsymbol{\theta}\le\boldsymbol{\theta}_{\max},\ \left\|\boldsymbol{\theta}-\boldsymbol{\theta}^l\right\|\le\rho_l$$

where ρ_l is the trust region radius for the *l*-th iteration, used to limit the search range for a single rotation. After obtaining the candidate rotation parameters, the objective function value for the true point cloud gap, $J_\theta(\boldsymbol{\theta}_{\text{cand}}^l)$, is recalculated. If the candidate parameters reduce the objective function value, the rotation update is accepted:

$$\boldsymbol{\theta}^{l+1}=\boldsymbol{\theta}_{\text{cand}}^l$$

Otherwise, the current search center remains unchanged, and the trust-region radius is reduced:

$$\rho_{l+1}=\kappa\rho_l,\quad 0<\kappa<1$$

As the iteration progresses, the trust-region radius gradually decreases, allowing the rotation fine adjustment to transition from small-angle probing over a large range

to fine adjustments. This process does not rely on the gradient of the objective function and can complete the local optimization of the three rotation parameters with fewer function evaluations. It is therefore suitable for the low-dimensional, bounded, derivative-free local optimization of gap uniformity after insertion-depth correction in this study.

After obtaining the optimal rotation increment $\boldsymbol{\theta}_{\text{opt}}^{(r)}$, update the pose matrix:

$$R^{(r+1)} = R_{\Delta}\left(\boldsymbol{\theta}_{\text{opt}}^{(r)}\right) R^{(r)}$$

Then proceed to the next iteration, repeating the insertion depth and rotation gap uniformity optimization. The fine pose adjustment process terminates when the average gap on each assembly surface approaches the target value, the standard deviation of in-plane gaps meets the requirements, the minimum gap satisfies the safety margin, or the decrease in the objective function over two consecutive iterations is less than the threshold. Let the rotation matrix and translation vector at the end of fine pose adjustment be R_{opt} and t_{opt}, respectively. Then, the final pose transformation matrix can be expressed as:

$$T_{\text{opt}} = \begin{bmatrix} R_{\text{opt}} & t_{\text{opt}} \\ 0 & 1 \end{bmatrix}$$

whereT_{opt} is the target assembly pose obtained through point cloud gap optimization, and serves as the input for subsequent trajectory planning.

3 Multi-Axis Cooperative Motion Trajectory Planning for Fully-Actuated Positioners

The target assembly pose obtained from the measured point clouds only characterizes the final geometric state of the wing and must be further converted into motion commands executable by each axis of the fully-actuated positioner. To this end, this section employs fifth-order polynomial interpolation to generate a smooth six-degree-of-freedom trajectory for the wing, ensuring that the motion process satisfies constraints such as trajectory continuity, smooth velocity, reachability, and multi-axis synchronization[15]; subsequently, through inverse kinematic mapping, the overall wing trajectory is decomposed into position commands for each axis of the positioner.

3.1 Assembly-Space Trajectory Planning

Let the initial pose of the wing in the assembly coordinate system be:

$$\boldsymbol{\eta}_0 = \left[x_0, y_0, z_0, \alpha_0, \beta_0, \gamma_0\right]^T$$

The target assembly pose obtained in Section 2 is T_{opt}. Based on the pose difference between the initial pose and the target assembly pose, the optimal pose adjustment required for the wing to move from the initial state to the target state is $\Delta\boldsymbol{\eta}_{\text{opt}}$. Therefore, the target pose is:

$$\boldsymbol{\eta}_f = \boldsymbol{\eta}_0 + \Delta\boldsymbol{\eta}_{\text{opt}}$$

To avoid sudden changes in velocity and acceleration during startup and stopping, a fifth-order polynomial trajectory function is adopted:

$$\tau = \frac{t}{T}, \quad s(\tau) = 10\tau^3 - 15\tau^4 + 6\tau^5$$

This function ensures continuity at the start and end positions, with both initial and final velocities and accelerations equal to zero. The desired pose of the wing at any given time is:

$$\boldsymbol{\eta}_d(t) = \boldsymbol{\eta}_0 + s(\tau)\left(\boldsymbol{\eta}_f - \boldsymbol{\eta}_0\right)$$

The corresponding velocity and acceleration are:

$$\dot{\boldsymbol{\eta}}_d(t) = \frac{1}{T}\frac{ds(\tau)}{d\tau}\left(\boldsymbol{\eta}_f - \boldsymbol{\eta}_0\right), \ \ddot{\boldsymbol{\eta}}_d(t) = \frac{1}{T^2}\frac{d^2 s(\tau)}{d\tau^2}\left(\boldsymbol{\eta}_f - \boldsymbol{\eta}_0\right)$$

where:

$$\frac{ds}{d\tau} = 30\tau^2 - 60\tau^3 + 30\tau^4, \ \frac{d^2 s}{d\tau^2} = 60\tau - 180\tau^2 + 120\tau^3$$

Since the magnitude of pose adjustments during wing-fuselage assembly is typically small, this paper performs synchronous interpolation of the translational and Euler angle components to generate a smooth six-degree-of-freedom pose trajectory. When the trajectory does not meet the requirements for velocity, acceleration, or assembly safety distance, adjustments can be made by extending the planning time, reducing the magnitude of single-step pose adjustments, or adopting a segmented planning approach.

3.2 Inverse Kinematics Mapping of Positioners

After obtaining the desired six-degree-of-freedom pose trajectory for the wing, the overall motion of the wing must be mapped to position commands for the individual axes of multiple fully-actuated positioners. Let the wing be supported by n positioners, and let the coordinates of the connection point between the i-th positioner and the wing in the wing's local coordinate system be $\mathbf{b}_i$. The rotation matrix and translation vector corresponding to the desired wing pose are $R_d(t)$ and $\mathbf{p}_d(t)$, respectively. Then, the desired position of the i-th support point in the assembly coordinate system is:

$$\mathbf{r}_i^d(t) = \mathbf{p}_d(t) + R_d(t)\mathbf{b}_i$$

Let the origin of the base of the i-th positioner be $\mathbf{o}_i$, and let the rotation matrix of its local coordinate system relative to the assembly coordinate system be R_i. If the positioner is a three-degree-of-freedom orthogonal motion mechanism, then the axial displacement command for this positioner is:

$$\mathbf{q}_i(t) = R_i^T\left[\mathbf{r}_i^d(t) - \mathbf{o}_i\right]$$

Combining all positioner displacement commands yields the multi-axis motion commands for the fully-actuated positioning system:

$$\mathbf{Q}(t) = \left[\mathbf{q}_1^T(t), \mathbf{q}_2^T(t), \cdots, \mathbf{q}_n^T(t)\right]^T$$

In the actual control system, the continuous trajectory is discretized based on the control cycle to obtain the sequence of position commands at each control instant. Since the commands for each axis are derived from the same six-degree-of-freedom trajectory of the wing, all positioners start, operate, and reach their target positions synchronously under unified time parameters, thereby ensuring the geometric coordination and motion stability of the overall wing pose adjustment process.

4 Real-Time Data Acquisition, Storage, and Monitoring During the Assembly Process

To ensure the smooth movement of the wing and assembly safety during the pose adjustment process, real-time monitoring of the positioner operating status and the force conditions at the support points is required. This section introduces methods for high-frequency force and position data acquisition, storage, and visual monitoring tailored for fully-actuated wing-fuselage assembly. These methods are used to record the positional status of each positioner and the 3D force variations at the support points, providing data support for safety assessment and quality traceability during the assembly process.

4.1 Data Acquisition and Storage Architecture

Real-time data collected during the wing-fuselage assembly process primarily includes positioner motion data, 3D force sensor data, and equipment status data. Positioner motion data is sourced from the programmable logic controller (PLC) of the fully-actuated positioner and mainly comprises the commanded positions and actual feedback positions, operational status, and alarm status of each motion axis; 3D force data is sourced from the 3D force sensor installed beneath the positioner's ball joint; equipment status data primarily includes the operational status of each motion axis and the operational status of the 3D force sensor.

To address the need for unified acquisition, transmission, and storage of the aforementioned real-time data, this paper establishes a real-time data acquisition workflow tailored to the fully-actuated wing-fuselage assembly process. The positioner PLC and the 3D force sensor are used to acquire the positioner's multi-axis motion status data and the force status data at the support points, respectively, and feed the underlying device data into KEPServerEX Version 6 (PTC Inc., USA). KEPServerEX uniformly manages the communication interfaces, variable addresses, and data types of different devices, mapping field device variables to standardized OPC Unified Architecture (OPC UA) variable nodes. This approach abstracts away differences in underlying device protocols and provides a unified data access interface for the host computer. On the host computer side, the Telegraf data agent is deployed. It periodically reads real-time variables via the OPC UA input plugin and writes the collected results to the TDengine time-series database in a predefined data format, enabling continuous collection and storage of high-frequency force and position status data throughout the entire fully-actuated assembly process [16].

Each time-series data record consists of a timestamp, a tag, and data fields. Positioner position data can be represented as:

$$D_p = \{T, Tag_p, Field_p\}$$

where T is the timestamp, Tag_p= *{task_id, positioner_id, axis_id, side_id}*, and $Field_p$= *{q_cmd, q_act, q_err, axis_status, alarm_code}*. This type of data is used to record the operational status of each positioner's motion axes during the assembly process.

The 3D force sensor data can be represented as:

$$D_w = \{T, Tag_w, Field_w\}$$

where Tag_w= *{task_id, sensor_id, positioner_id, side_id}*, $Field_w$=*{*F_x*,* F_y*,* F_z*, sensor_status}*. To mitigate the effects of sensor zero drift, the preload from the wing's own weight, and the initial support state, the initial values of the 3D force sensors are recorded prior to formal assembly. During monitoring, the focus is on analyzing force increments relative to the initial state. If the compensated data is written directly to the database, the field can be expanded to $\Delta F_x, \Delta F_y, \Delta F_z$. Through the aforementioned time-series data structure, the position of the positioner, the 3D force at the ball-and-socket support points, and the equipment status can all be stored and correlated along a unified timeline. After assembly is complete, the entire process data can be queried based on the assembly task number to reconstruct the positioner's motion trajectory, changes in forces at the support points, and the equipment's operational status, thereby providing a data foundation for analyzing wing-fuselage assembly quality, reviewing processes, and establishing individual assembly records.

4.2 Force-Position Coordinated Monitoring and Visualization

After completing the collection and storage of high-frequency process data, this paper uses Grafana 10.4.3 (Grafana Labs, USA) to build a visualization interface for the wing-fuselage assembly process. This interface provides an intuitive display of the positioner's motion and the 3D force changes at the support points, supporting the monitoring of the assembly process status. Grafana was configured with TDengine 3.4.1 (TAOS Data, China) as the data source to retrieve real-time position data from each axis of the positioner and data from the 3D force sensors, presenting the assembly process in the form of time-series curves.

The visualization interface primarily consists of two parts: the position curve and the 3D force curve. The

position curve displays the real-time positions of each motion axis and their changes over time, reflecting the motion state of the positioner during the assembly process; the 3D force curve displays the changes in the three components (F_x , F_y , andF_z) at the ball-socket support point, reflecting the support force state during the assembly process.

Position data is sourced from real-time feedback from the positioner's PLC, recording the actual displacement of each motion axis during the assembly process; the position time-series curve can be used to assess the continuity and smoothness of motion, as well as whether there are any significant stalls or abnormal fluctuations. 3D force data is collected by a 3D force sensor installed beneath the ball socket of the positioner. The sensor's initial values are recorded prior to assembly, and the monitoring focuses on force changes relative to the initial state. If a force curve in a particular direction exhibits a significant peak or sustained increase, this typically indicates a change in the force state at the support point, suggesting the presence of internal forces due to pose adjustment.

Grafana reads and displays position and force data stored at high frequency in TDengine in real time, enabling operators to intuitively monitor the positioner's motion and changes in the force applied to the ball-and-socket support points. After assembly is complete, the system can replay and trace the positioner's motion trajectory and 3D force changes based on the high-frequency process data in the database, providing data support for anomaly analysis of the assembly process.

5 Comprehensive Experiments and Results Verification

To validate the effectiveness of the fully-actuated pose adjustment method for wing-fuselage assembly via point-cloud gap optimization, a wing-fuselage assembly experimental platform was established. Experimental validation was conducted from two aspects: the smoothness of the assembly process and the effectiveness of assembly gap improvement.

5.1 Experimental Setup

This experiment was conducted using the wing-fuselage assembly test platform shown in Fig. 4. The platform primarily consists of a fuselage mock-up, a wing mock-up, multi-axis fully-actuated positioners, a laser tracker, a 3D force sensor, and ERS reference points. During the experiment, the fuselage mock-up served as the fixed reference for the entire wing-fuselage assembly process and was securely mounted on one side of the platform, maintaining a fixed position throughout the scanning and assembly procedures. The initial position of the ball center on the wing mock-up ball joint had been calibrated within the aircraft component assembly coordinate system. Through the coordinated support and drive of multiple fully-actuated positioners, the wing assembly area was gradually inserted into the corresponding assembly area of the fuselage mock-up as the positioners moved in coordination, thereby achieving precise adjustment of the wing pose and successful wing-fuselage assembly.

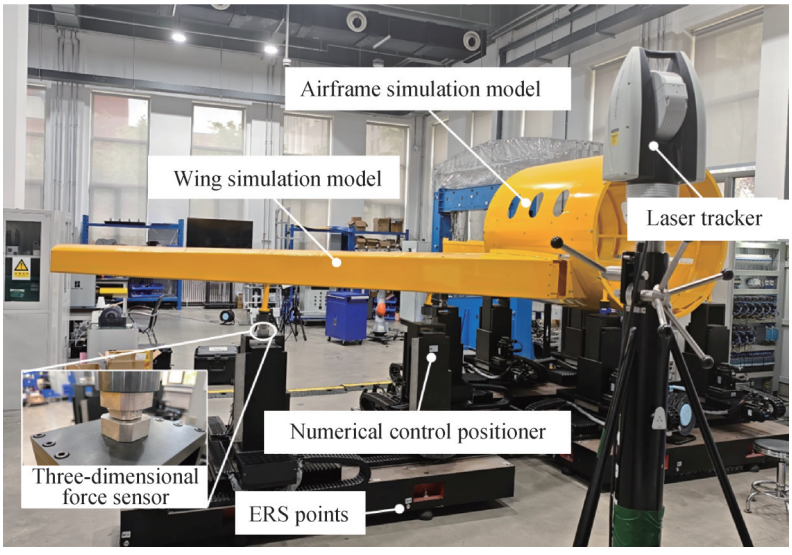

Fig.4 Wing-fuselage assembly test platform

To optimize the gap based on measured point cloud data, prior to the experiment, a laser tracker equipped with a handheld scanner was first used to perform high-precision 3D scanning of the assembly frame area between the fuselage and wing mock-ups. The scanning scene is shown in Fig. 5. Using ERS reference points pre-deployed at the experimental site, the laser tracker converted the collected local point cloud data into the aircraft component assembly coordinate system to ensure spatial consistency across multiple scan data sets. Based

on this, the raw point cloud data underwent preprocessing steps including denoising, simplification, and feature extraction, resulting in the point cloud model of the experimental object shown in Fig. 6. This model accurately reproduces the spatial geometric features of the assembly frame and provides critical data input for subsequent gap modeling and target pose optimization.

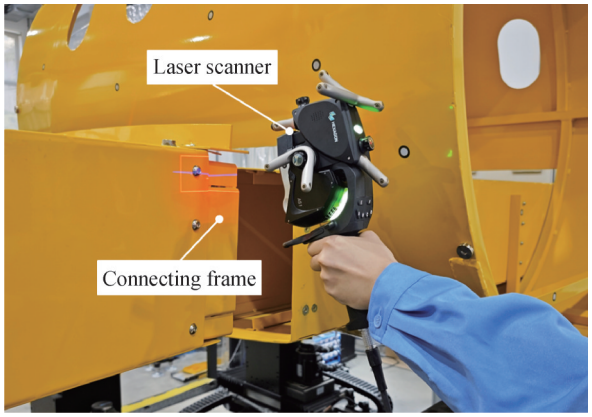

Fig.5 On-site 3D scanning of the assembly-frame region using a laser tracker

(a) Point cloud model of the fuselage mock-up assembly frame

(b) Point cloud model of the wing mock-up assembly frame

Fig.6 Point cloud models of the fuselage and wing assembly frames

During the validation phase, two comparative assembly conditions were established to evaluate the effectiveness of the proposed method. The first condition was the traditional manual assembly condition, which followed a conventional pose-adjustment and docking procedure based on the positional relationships of theoretical key measurement points. Specifically, the operator first manually adjusted the positioners according to the nominal spatial relationships of the key measurement points specified in the theoretical CAD model, thereby rotating the wing mock-up toward the target assembly pose. Subsequently, the wing mock-up was translated along the assembly direction to the target assembly position according to the positional relationships of the key measurement points. Assembly was considered complete when the measured positions of all key measurement points satisfied the prescribed positional tolerances. In this condition, gap measurements were used only to evaluate the final assembly result after pose adjustment had been completed; they were not used as input for pose optimization or as a closed-loop control criterion during the manual adjustment process. Therefore, the traditional method uses the positional conformity of discrete key measurement points as the primary assembly criterion and does not explicitly control the global gap distribution or in-plane gap uniformity of the mating surfaces, making it difficult to ensure the overall uniformity of the actual assembly gaps.

The second condition was the point-cloud-gap-optimized assembly condition proposed in this paper. The same key measurement points and positional-tolerance requirements as those used in the traditional manual assembly condition were retained to ensure comparable assembly requirements. Before pose adjustment, measured point-cloud data were acquired to construct a multi-surface global gap model and determine the optimized target assembly pose. The optimized pose parameters were then converted into motion-control commands to drive the wing positioners for fully-actuated pose adjustment. Thus, unlike the traditional manual condition, the measured gap distribution was incorporated into target-pose determination before physical adjustment, rather than being used only for post-assembly evaluation. After assembly under both conditions, the actual assembly gaps were measured using the same vernier feeler gauge with a range of 0-15 mm and a resolution of 0.2 mm to quantitatively evaluate the assembly performance of the two methods.

To ensure representativeness of the assembly direction, the upper and right assembly surfaces were selected as evaluation targets for the gap optimization results. The specific measurement scheme is shown in Fig. 7. During measurement, test points were sequentially arranged at 50-mm intervals along the length of the assembly frame, and the values at each point were recorded along the gap direction. To minimize manual measurement errors, each measurement point was measured three times, and the average value was taken as the final result. By comparing the uniformity of gap distribution under the two operating conditions, the optimization effect of the proposed method was quantitatively evaluated; simultaneously, combined with the positioner displacement and 3D force data collected synchronously under operating condition 2, the motion stability of the fully-actuated pose adjustment process was further verified.

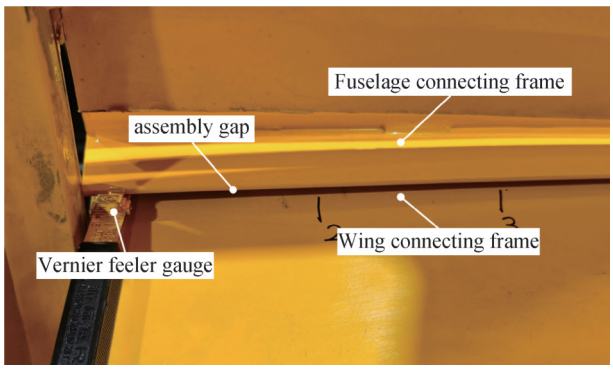

Fig.7 Schematic diagram of assembly gap measurement between assembly frames

5.2 Quantitative Evaluation of Process Stability During Fully-Actuated Pose Adjustment

To quantitatively evaluate the execution stability of the point-cloud-optimized target pose during fully-actuated pose adjustment, the position commands issued by the PLC, the feedback positions of the motion axes, and the three-dimensional forces at the support points were synchronously recorded and archived. The position data were acquired through the PLC, whereas the three-dimensional force data were measured by force sensors mounted beneath the ball joints of the positioners and stored in the time-series database through the data-acquisition and storage system described in Section 4. Using common timestamps as the reference, the commanded positions, feedback positions, and three-dimensional support-force data were synchronized for analysis.

For the i-th motion axis, the position-tracking error at time t is defined as

$$e_i(t)=q_i^{\mathrm{act}}(t)-q_i^{\mathrm{cmd}}(t)$$

where $q_i^{\mathrm{cmd}}(t)$ and $q_i^{\mathrm{act}}(t)$ denote the real-time position command issued by the PLC and the actual feedback position of the corresponding positioner axis, respectively. The mean absolute tracking error and the maximum absolute tracking error are used to evaluate the trajectory-tracking performance of each motion axis:

$$\mathrm{MAE}_i=\frac{1}{N}\sum_{t=1}^{N}\left|e_i(t)\right|$$

$$e_{i,\max}=\max_t\left|e_i(t)\right|$$

Fig. 8 presents the actual feedback-position curves of representative motion axes during pose adjustment and assembly, providing a direct visualization of the continuity and final convergence of the coordinated multi-axis motion process. Table 1 summarizes the command-to-feedback tracking-error statistics for the 9 motion axes. For the experimental platform considered in this study, the tracking performance of an individual motion axis was regarded as acceptable when its mean absolute tracking error did not exceed 0.020 mm and its maximum absolute tracking error did not exceed 0.050 mm. These limits were adopted as conservative process-control thresholds and were set below the 0.2 mm resolution used for post-assembly gap verification, so that motion-tracking deviations would not dominate the subsequent gap-evaluation results. The mean absolute tracking errors of the motion axes range from 0.006 mm to 0.012 mm, whereas the maximum absolute tracking errors range from 0.020 mm to 0.039 mm. Therefore, all nine motion axes satisfy the specified tracking-performance criteria. These results indicate that the positioner axes closely follow the PLC-issued motion commands and achieve stable coordinated execution of the point-cloud-optimized target pose.

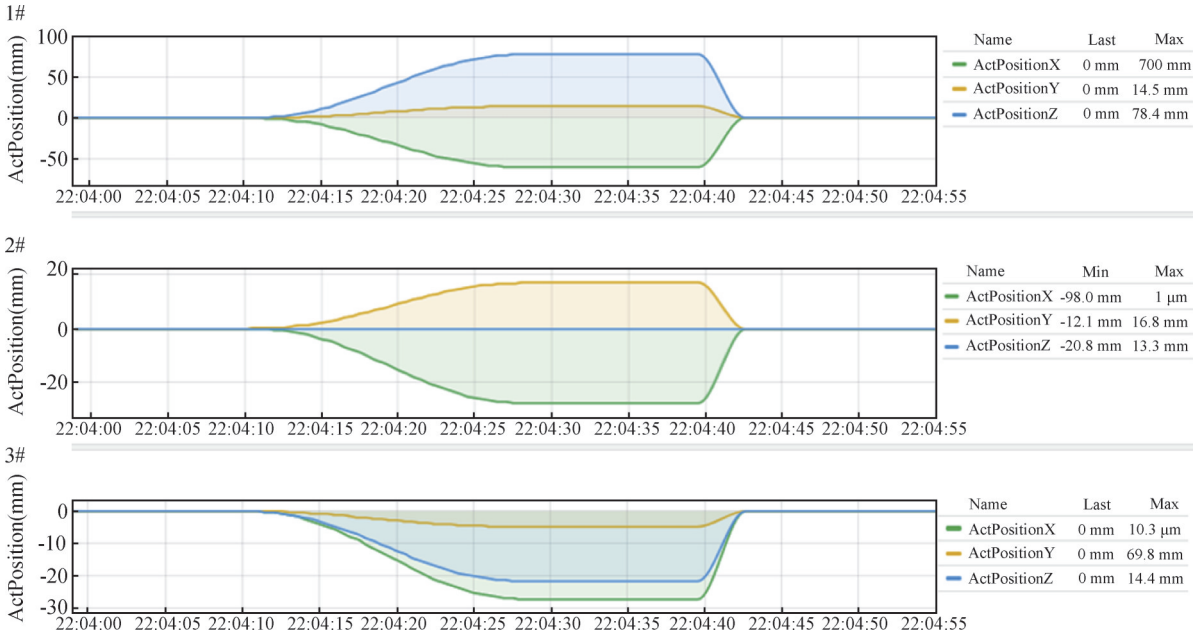

Fig.8 Position curves of the positioner motion axes during the assembly process

To characterize support-force variations during pose adjustment, the three-dimensional force readings at the beginning of the formal pose-adjustment stage were used as the baseline. The force increment in direction d is defined as

$$\Delta F_d(t)=F_d(t)-F_d(t_0),\quad d\in\{x,y,z\}$$

where $F_d(t_0)$ denotes the initial force value in the corresponding direction at the beginning of formal pose adjustment. The standard deviation and maximum absolute value of the force increment were calculated to characterize the force fluctuations at each support point:

$$\sigma_{F_d}=\sqrt{\frac{1}{N}\sum_{t=1}^{N}\left[\Delta F_d(t)-\overline{\Delta F_d}\right]^2}$$

Table 1 Command-to-feedback tracking-error statistics of motion axes during fully-actuated pose adjustment

Positioner No.	Motion axis	Mean absolute tracking error (MAE)/mm	Maximum absolute tracking error/mm
1	Axis_0	0.006	0.021
1	Axis_1	0.008	0.026
1	Axis_2	0.010	0.034
2	Axis_3	0.007	0.022
2	Axis_4	0.009	0.029
2	Axis_5	0.011	0.037
3	Axis_6	0.006	0.020
3	Axis_7	0.010	0.030
3	Axis_8	0.012	0.039

$$\Delta F_{d,\max} = \max_t \left| \Delta F_d(t) \right|$$

For the experimental platform considered in this study, the support-force variation of each force component at a support point was regarded as acceptable when the standard deviation of its force increment did not exceed 1 N and its maximum absolute force increment did not exceed 150 N. These platform-level process-control thresholds were determined with reference to the baseline noise of the corresponding force-sensor channel and the allowable support-force variation of the experimental platform. In addition, no sustained monotonic increase or abrupt peak exceeding the corresponding threshold was permitted during pose adjustment. The relatively larger force increments observed at Positioner 3 were mainly attributed to the redistribution of support loads among the positioners caused by the change in component pose during coordinated adjustment. As shown in Table 2 and Fig. 9, the measured support-force variations satisfied the specified criteria, indicating that no evident abnormal constraint interaction occurred during the recorded pose-adjustment process.

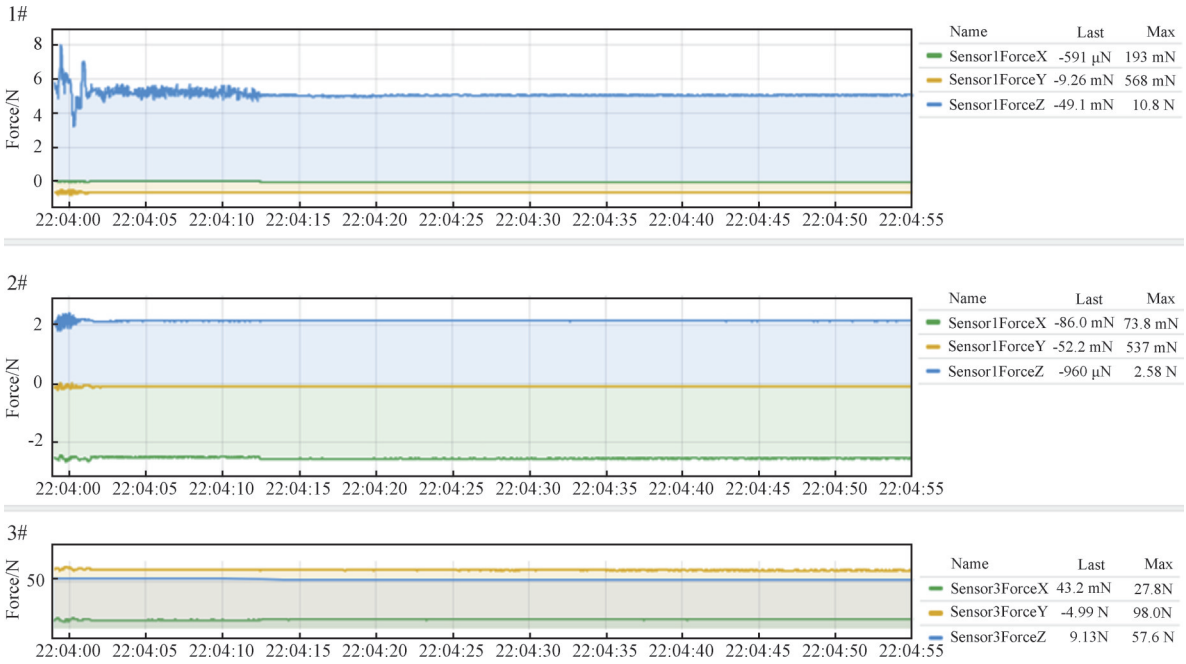

Fig.9 Three-dimensional force variation curves during the assembly process

Table 2 Statistics of three-dimensional force variations at the positioners during fully-actuated pose adjustment

Positioner No.	Force component	Standard deviation of force increment/N	Maximum absolute force increment/N
1	(F_x)	0.03	0.193
1	(F_y)	0.02	0.568
1	(F_z)	0.42	10.8
2	(F_x)	0.02	0.0738
2	(F_y)	0.01	0.537
2	(F_z)	0.08	2.58
3	(F_x)	0.35	27.8
3	(F_y)	0.38	98.0
3	(F_z)	0.01	57.6

In summary, all nine motion axes satisfied the specified tracking-performance criteria, with mean absolute tracking errors below 0.020 mm and maximum absolute tracking errors below 0.050 mm. In addition, the standard deviations of the three-dimensional support-force increments were below 1 N, and the maximum absolute force increments were below 150 N for all monitored force components. These quantitative results indicate that the positioner axes stably followed the PLC-issued motion commands and that the support points did not exhibit evident abnormal force fluctuations during the recorded pose-adjustment process. No sustained abnormal force increase, abrupt force peak, or evident motion anomaly was observed, indicating that no apparent abnormal constraint interaction or local

interference occurred during the monitored process. Therefore, the proposed method can convert the point-cloud-optimized target pose into a coordinated multi-axis physical execution process with stable motion performance, while providing quantitative data support for assembly-process monitoring and quality traceability.

5.3 Assembly Accuracy and Gap Verification

To verify the effectiveness of this method in improving the uniformity of assembly gaps, a comparative analysis was conducted on measured data from two sets of operating conditions: traditional assembly and point cloud gap-optimized assembly. According to the measurement plan, 11 measurement points (designated as Top 1–Top 11) were arranged on the upper assembly surface, and 5 measurement points (designated as Right 1 – Right 5) were arranged on the right assembly surface. The measured gap results for each point are shown in Fig. 10.

As shown in Fig. 10, the gap values obtained using the traditional method exhibit significant fluctuations depending on the spatial location of the measurement points, with some local areas showing a sharp decrease in gap. This result indicates that satisfying the positional tolerances of discrete key measurement points does not explicitly control the global gap distribution or in-plane gap uniformity of the mating surfaces. In contrast, after applying the proposed point cloud gap optimization method, the gap curves for both the upper and right assembly surfaces became noticeably smoother, and local abrupt changes were effectively suppressed, intuitively demonstrating that this method can significantly improve the global uniformity of gaps after actual assembly.

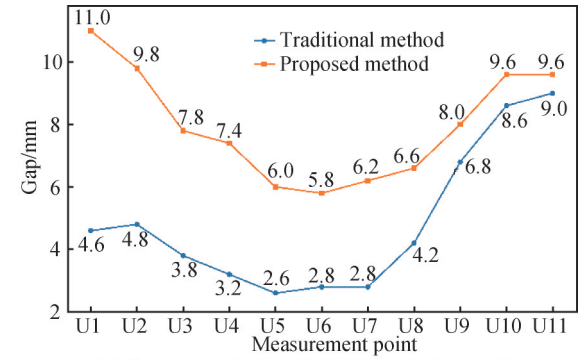

(a) Gap comparison on the upper assembly surface

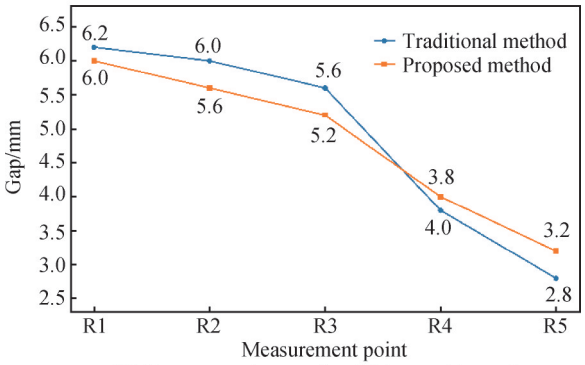

(b) Gap comparison on the right assembly surface

Fig.10 Comparison of measured assembly gaps between the traditional method and the proposed method

To further evaluate the uniformity of the gap distribution, the average gap, minimum gap, maximum gap, and standard deviation for the upper and right assembly surfaces were calculated; the results are shown in Table 3.

Table 3 Comparison of assembly-gap statistics between the traditional manual method and the point-cloud-gap-optimized method

Assembly Surface	Method	Average gap/mm	Minimum gap/mm	Maximum gap/mm	Standard deviation/mm
Upper surface	Traditional method	4.84	2.6	9.0	2.19
	Proposed method	7.98	5.8	11.0	1.70
Right surface	Traditional method	4.88	2.8	6.2	1.34
	Proposed method	4.80	3.2	6.0	1.04

As shown in Table 3, compared with the traditional method, the standard deviations of the gaps on the upper and right assembly surfaces under the proposed method decreased from 2.19 mm and 1.34 mm to 1.70 mm and 1.04 mm, respectively, indicating a reduction in in-plane gap fluctuations. Meanwhile, the minimum gaps on the upper and right assembly surfaces increased from 2.6 mm and 2.8 mm to 5.8 mm and 3.2 mm, respectively, indicating that local small-gap regions were improved and that the risk of potential contact or interference was reduced.

By integrating the spatial distribution of measurement points with global statistical metrics, the proposed method establishes a global gap model from measured multi-source point clouds and optimizes the target assembly pose. The experimental results demonstrate its effectiveness in improving the uniformity of the measured assembly gaps and reducing the occurrence of local small-gap regions.

6 Conclusions

This paper proposes a fully-actuated pose adjustment method for aircraft wing-fuselage assembly via point-cloud gap optimization, achieving a complete workflow from point cloud acquisition in the assembly region, global gap modeling, and target pose optimization to fully-actuated trajectory execution and in-process data monitoring. Based on the measured point-cloud data, a global gap field is constructed along prescribed region-wise assembly directions, thereby incorporating the

actual geometric condition of the assembly frames into assembly-gap evaluation and pose optimization. By combining coarse pre-alignment with fine pose adjustment and decoupling insertion-depth correction from rotational gap-uniformity optimization, the stability and execution feasibility of point-cloud gap optimization are improved. Experimental results show that, compared with the traditional assembly method, the proposed method reduces gap fluctuations at measurement points on typical assembly surfaces, decreases the in-plane gap dispersion, and makes the actual assembly gap distribution more uniform. During pose-adjustment execution, the positioner motion curves remained continuous and smooth, and no evident abnormal fluctuation was observed in the three-dimensional support forces at the support points, further verifying the effectiveness of the proposed method for wing-fuselage gap optimization and fully-actuated pose adjustment.

Author Contribution:

Xiao Xu, Conceptualization, Data Curation, Formal Analysis, Methodology, Software, Visualization, Writing-Original Draft, Investigation, Writing-Review & Editing. Runze Liu, Conceptualization, Data Curation, Formal Analysis, Methodology, Writing-Original Draft, Investigation, Writing-Review & Editing. Yongkang Lu, Conceptualization, Methodology, Funding Acquisition, Supervision, Writing-Original Draft, Writing-Review & Editing. Yang Zhang, Supervision, Validation. Wei Liu, Supervision, Validation. Qihang Chen, Data Curation, Formal Analysis, Software. Haoyu Wu, Data Curation, Formal Analysis, Investigation.

Acknowledgments:

The authors acknowledge Dalian University of Technology and COMAC Shanghai Aircraft Manufacturing Co., Ltd. for supporting this research work.

Foundation Information:

This work was supported by the Young Elite Scientists Sponsorship Program by CAST (Grant No. YESS20240732) and in part by the National Science Foundation for Young Scientists of China (Grant No. 52405581) and the Innovation Foundation of National Commercial Aircraft Manufacturing Engineering Technology Research Center (Grant No. COMAC-SFGS-2026-349).

Data Availability:

Data will be made available on request.

Conflicts of Interest:

The authors declare no competing interests.

Dates:

Received 27 May 2026; Accepted 01 July 2026; Published online 10 July 2026

References

[1] Chen Z, Du F, Tang X, et al. A framework of measurement assisted assembly for wing-fuselage alignment based on key measurement characteristics[J]. *International Journal of Manufacturing Research* , **2015**, 10(2): 107-128.

[2] Maropoulos P G, Muelaner J E, Summers M D, et al. A new paradigm in large-scale assembly—research priorities in measurement assisted assembly[J]. *The International Journal of Advanced Manufacturing Technology*, **2014**, 70(1): 621-633.

[3] Zhao X, Zhang C, Xu L, et al. Gap measurements in aerospace engineering[J]. *Sensors* , **2025**, 25(10): 3059.

[4] Long K, Xie Q, Lu D, et al. Aircraft skin gap and flush measurement based on seam region extraction from 3D point cloud[J]. *Measurement* , **2021**, 176: 109169.

[5] Dai J, Wei M, Xie Q, et al. Aircraft seam feature extraction from 3D raw point cloud via hierarchical multi-structure fitting[J]. *Computer-Aided Design* , **2021**, 130: 102945.

[6] Wang Y, Liu Y, Xie Q, et al. Density-invariant registration of multiple scans for aircraft measurement[J]. *IEEE Transactions on Instrumentation and Measurement* , **2020**, 70: 1-15.

[7] Wang Y, Liu Y, Chen H, et al. Combined measurement based wing-fuselage assembly coordination via multiconstraint optimization[J]. *IEEE Transactions on Instrumentation and Measurement* , **2022**, 71: 1-16.

[8] Wang Q, Dou Y, Li J, et al. An assembly gap control method based on posture alignment of wing panels in aircraft assembly[J]. *Assembly Automation* , **2017**, 37(4): 422-433.

[9] Sun Z, Pan Z, Shangguan J, et al. A posture alignment-based methodology for gap optimization of aircraft composite panel assembly[J]. *Aerospace Science and Technology* , **2023**, 140: 108442.

[10] Chang Z, Ren Y, Li X, et al. Assembly deformation prediction of aircraft composite panel considering manufacturing variation and actual assembly process[J]. *The International Journal of Advanced Manufacturing Technology* , **2024**, 135 (7): 3811-3825.

[11] Zhang B, Yao B, Ke Y. A novel posture alignment system for aircraft wing assembly[J]. *Journal of Zhejiang University-SCIENCE A* , **2009**, 10(11): 1624-1630.

[12] Chu W, Huang X. Self-calibration method of NC positioner for posture adjustment[J]. *The International Journal of Advanced Manufacturing Technology* , **2022**, 119(11): 7669-7683.

[13] Chu W, Li G, Li S, et al. Posture adjustment method of large aircraft components based on multiple numerical control positioners[J]. *The International Journal of Advanced Manufacturing Technology* , **2023**, 126(5): 2159-2174.

[14] Powell M J D. The BOBYQA algorithm for bound constrained optimization without derivatives[R]. Cambridge NA Report NA2009/06, University of Cambridge, Cambridge, **2009**, 26(26-46): 1.

[15] Jin H, Liu D. Two-point positioning and pose adjustment method for automatic assembly of barrel-type cabin[J]. *China Mechanical Engineering* , **2018**, 29(12): 1467-1474.

[16] Garcia A, Oregui X, Franco J, et al. Time series manufacturing data edge monitoring and visualization to support industrial maintenance teams[J]. *SN Computer Science* , **2023**, 5(1): 131.